SolarPACES 2024, 30th International Conference on Concentrating Solar Power, Thermal, and Chemical Energy Systems

Solar Fuels and Chemical Commodities

https://doi.org/10.52825/solarpaces.v3i.2433

© Authors. This work is licensed under a Creative Commons Attribution 4.0 International License

Published: 09 Oct. 2025

# High Concentration Optical System for Solar Fuel Production via Cerium Oxide Thermochemical Cycle

Alejandro González Silvestre<sup>1,\*</sup> , Gioele di Marcoberardino<sup>2</sup>, and Marco Binotti<sup>1</sup>

<sup>1</sup>Politecnico di Milano, Italy

<sup>2</sup>University of Brescia, Italy

\*Correspondence: Alejandro González Silvestre, alejandro.gonzalez@polimi.it

**Abstract.** The integration of solar energy into hydrogen fuel production marks a key step towards sustainable energy. This study, which is part of a Marie Skłodowska-Curie Action called "TOPCSP", aims to optimize the design of a concentrated solar power system tailored for high-temperature applications such as thermochemical cycles for hydrogen production. The system features a point-focus tower with compound parabolic concentrators as secondary concentrator to maximize solar radiation capture and to minimize receiver thermal losses, enhancing the efficiency of the solar-to-fuel conversion. Hydrogen is produced through a two-step thermochemical cycle using non-stoichiometric ceria, designed for high efficiency and scalability. Through theoretical modeling and simulations, this work presents an optimal optical configuration that boosts hydrogen production rates and reduces overall system costs.

**Keywords:** Solar Fuels, High Concentration Optical System, Cerium Oxide Thermochemical cycle, Hydrogen, CPC Cluster

# 1. Introduction: Thermochemical cycles

Thermochemical cycles for solar fuel production involve a series of chemical reactions that utilize heat from Concentrated Solar Power (CSP) to produce fuels such as hydrogen  $(H_2)$ , carbon monoxide (CO), syngas, methanol or others from various feedstocks. For instance, steam serves as the feedstock for hydrogen production, while  $CO_2$  is the feedstock for CO production. These cycles are promising candidates for solar fuel production due to their high theoretical efficiency, which is governed by solar energy absorption and Carnot efficiency, as shown in equation (1):

$$\eta_{solar-to-fuel}^{ideal} = \left(1 - \frac{\sigma T^4}{I \cdot CR_{eff}}\right) \left(1 - \frac{T_L}{T_H}\right) \tag{1}$$

From the analysis of this equation, it can be observed how increasing the concentration ratio (CR) and the temperature can lead to high efficiencies, as shown in *Figure 1*. However, while theoretical system efficiencies hover around 30%, actual experimental efficiencies remain significantly lower, around 5% [2]. The efficiency of a thermochemical cycle system,  $\eta_{SF}$ , can be expressed as equation (2):

$$\eta_{SF} = \frac{\dot{n}_{SF} \cdot \text{HHV}}{\dot{Q} + \frac{\dot{W}_{Tot}}{\eta_{Ph}}} \tag{2}$$

Where  $\dot{n}_{SF}$  is the solar fuel production rate, HHV is the higher heating value of the solar fuel,  $\dot{Q}$  is the total solar radiation entering the solar field,  $\dot{W}_{Tot}$  is the work of the auxiliaries required to run the cycle, and  $\eta_{th}$  is the electric to thermal efficiency of a conversion system (average typical value is approximately 0.4).

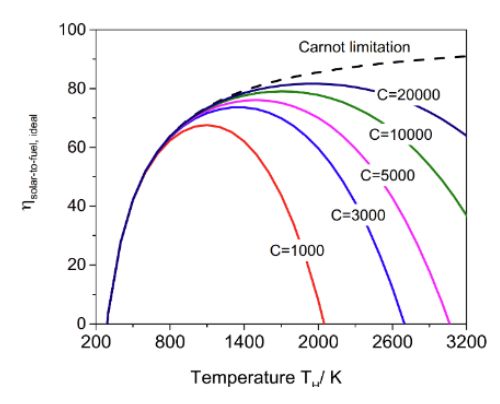


Figure 1. Theoretical Carnot efficiency of thermochemical cycles.[3]

#### 1.2 Two-step non-stoichiometric ceria cycle

These thermochemical cycles operate on redox reactions, where a metal oxide undergoes reduction in the first step and oxidation in the next, thereby completing the cycle. During the reduction step, oxygen is released, creating vacancies in the metal oxide. In the subsequent oxidation step, these vacancies are filled with oxygen from the supplied feedstock, typically steam or CO<sub>2</sub>, producing hydrogen, carbon monoxide, or syngas. Ceria-based oxides (see *Figure 2*) are particularly promising materials for this application due to their long-term thermal stability, high oxygen storage capacity, lower sintering, high melting point, and favorable redox reactivity [4]. The maximum temperature in this cycle occurs during the reduction step, ranging from 1400 to 1600 °C.

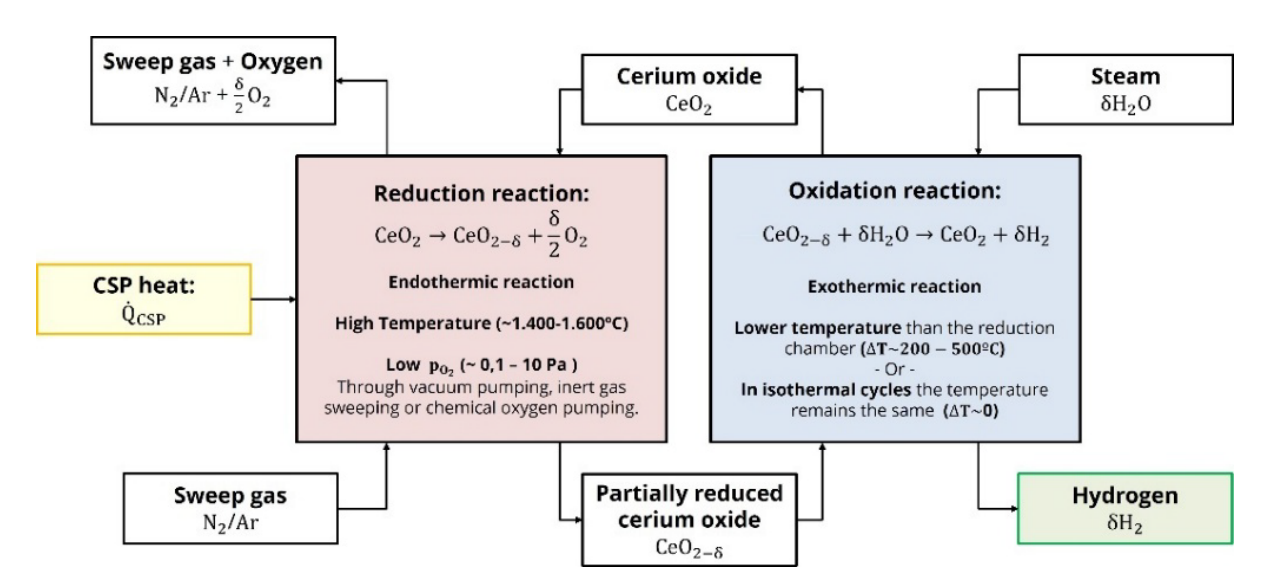


Figure 2. Two-step non-stoichiometric ceria cycle scheme for H2 production.

## 1.2 Compound Parabolic Concentrators (CPCs)

To achieve the high temperatures required for thermochemical cycles, high concentration ratios are necessary to minimize reradiation losses in the reduction reactor, as they allow smaller receiver apertures. Secondary concentrators, such as CPCs, can be employed to increase the concentration ratio of the heliostat field. CPCs are formed by revolving two parabolas, with the foci located at the lower edge of each other, as shown in *Figure 3*.

In a 2D configuration, this design ensures that any solar ray entering the CPC at a given semi-acceptance angle  $(\theta_{max})$  will exit through the outlet aperture, while the 3D revolution approximates this behavior. The theoretical concentration ratio of a CPC is dependent on the semi-acceptance angle and is given by equation (3). As the semi-acceptance angle decreases, the concentration ratio increases. However, a smaller semi-acceptance angle limits the heliostat field. For this application, semi-acceptance angles ranging from 10° (CR = 14.9) to 40° (CR = 2.42) are considered. Due to the elongated shape of CPCs required for these small acceptance angles, a single large CPC is impractical for "large apertures": as expressed in equation (4), the height is 6.66 times the inlet radius with  $\theta_{max} = 10^{\circ}$ . Instead, multiple smaller CPCs can be arranged in an array to cover larger aperture sizes while maintaining reasonable lengths. However, this array configuration increases the spillage due to the edges and gaps between the CPCs. Polygonal CPCs, such as square and hexagonal shapes, can be used to minimize spillage. Hexagonal CPCs were used since they are closer to the ideal revolution.

$$CR = \frac{1}{\sin^2(\theta_{max})} \tag{3}$$

$$h_{CPC} = f \frac{\cos(\theta_{max})}{\sin^2(\theta_{max})} = r_{out} \frac{(1 + \sin(\theta_{max})) \cdot \cos(\theta_{max})}{\sin^2(\theta_{max})} = r_{in} \frac{(1 + \sin(\theta_{max})) \cdot \cos(\theta_{max})}{\sin(\theta_{max})}$$
(4)

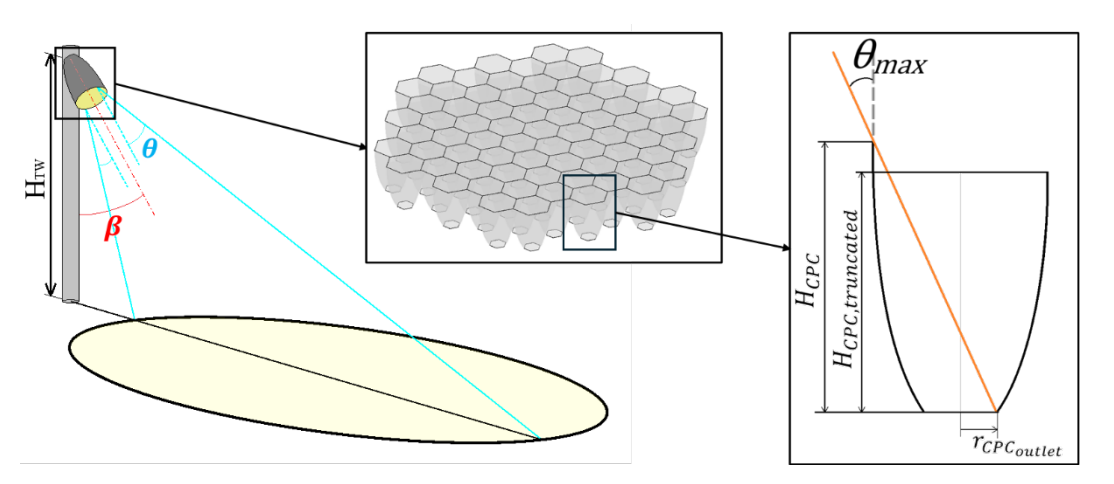
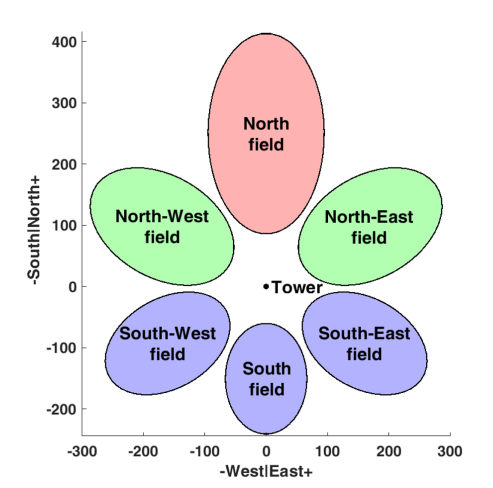


Figure 3. Heliostat field projection, CPC cluster and CPC geometry.

To limit the number of CPCs and reduce spillage at the edges, the maximum size of each CPC is constrained by the available quartz window size. A maximum diameter of 0.66 meters was identified from a 250 kW prototype reactor in the HYDROSOL project [5]. These windows will be installed at the CPC inlets to minimize the heat flux on their surfaces.

# 2. Methodology

The primary goal of this study is to determine the optimal configuration for a 100 MW<sub>th</sub> CSP tower system working at 1500 °C with three different setups: a single north-facing receiver, a combination of three receivers facing northwest, north, and northeast, and a combination of six receivers, as reported in *Figure 4*, facing northwest, north, northeast, southeast, south, and southwest. The power distribution among the receivers follows the study by Schmitz et al. (2006) [6]. The optical system optimization is divided into two parts, the primary concentrator (heliostat field) and the secondary concentrator (CPC array). The heliostat field is generated using Solar PILOT software [7], with inputs such as geographical location, design power, receiver position (tower height ( $h_{tower}$ ), tilt angle ( $\beta$ )) and acceptance angle (assumed equal to the CPC acceptance angle ( $2\theta_{max}$ )), heliostat size and design point Direct Normal Irradiance (DNI). For the optimization of the system, only the tower height, receiver tilt and acceptance angle are varied, while other parameters remain fixed to reduce computational time.



Single receiver power distribution			
Field	Power share	Thermal power	
N	100 %	100 MW	

3-receiver power distribution			
Field	Power share	Thermal power	
N	36 %	36 MW	
NW/NE	32 %	32 MW	

6-r	6-receiver power distribution			
Field	Thermal power			
N	22 %	22 MW		
NW/NE	19 %	19 MW		
SW/SE	14 %	14 MW		
S	12 %	12 MW		

**Figure 4.** Multiple receiver configurations projections and power share. Red: North facing field. Green plus Red: 3-receiver configuration fields. Blue plus Green plus Red: 6-receiver configuration fields.

**Table 1.** Fixed values and variable parameters considered in the optimization.

Design thermal power:	100 MW	Tower height:	<250 m
Design point DNI:	900 W/m <sup>2</sup>	Tower tilt:	20 – 90 °
Heliostat size:	10x10 m	CPC inlet radius:	0.300 m
Location:	Seville, Spain	CPC truncation:	10 %
Semi-acceptance angle:	10 – 40 °	Heliostat/CPC reflectance:	95 %

After generating the heliostat field, a ray-tracing simulation is performed by importing the field into SolTrace [7]. The receiver is modeled as a flat plate large enough to achieve a 100% intercept, as the CPCs' complex geometry cannot be easily exported and simulated in SolTrace. An analytical ray-tracing model developed in MATLAB® [8] is used to simulate the secondary concentrators. The data on the solar rays' position and direction hitting the flat plate is then imported into MATLAB® for CPC array optimization. The reduction reactor must reach temperatures of 1500 °C, so thermal reradiation is a significant loss mechanism. To address this, the optimal balance between intercept factor and aperture size is determined by maximizing the thermal energy supplied to the reactor. This is done by comparing the power received from the heliostat field for a variable intercept factor with the associated thermal losses from the aperture area, calculated using the Stefan-Boltzmann law ( $\sigma T^4$ ). Once the optimal aperture size is identified, the CPC array is simulated using the ray-tracing data to determine its efficiency. Following the optimization of both concentration stages, yearly simulations are conducted to calculate the annual thermal and optical efficiencies, leading to the estimation of the system's Levelized Cost of Heat (LCOH). The reference costs used are the standard values provided by SolarPilot, with a revised value for the heliostat field cost per square meter and adjustments for the receiver's power-dependent costs [9]. After completing the optical system optimization, the thermochemical cycle is simulated to determine hydrogen yield and cycle efficiency. The thermochemical cycle model, adapted and enhanced from S. Li et al. [10] and M. Binotti et al [11], incorporates the study of intermediate thermodynamic states along the solid/gas flow path within the reactor, based on the application of mass and species balances and of Gibbs' criterion, which is necessary to ensure that the reaction takes place spontaneously in every reaction section. Moreover, the heat exchanger network was modified properly, in particular the preheating and the sweep gas and steam production step. The literature model has a key issue with the heat exchanger on the oxidation side (HEX<sub>ox</sub>) in the water-splitting reactor, where the previous energy balance approach based on effectiveness is unsuitable due to variable heat capacity from phase changes. The revised model (see Figure 5) introduces a pinch-point temperature difference to ensure feasible heat transfer, leading to a significant reduction in thermal power exchange and a drop in water exit temperature, which ultimately requires additional solar power and results in decreased system efficiency. Additionally,

the heat recovery scheme is adjusted, assuming the purified nitrogen (sweep gas) is heated in a single step within the heat exchanger (HEX<sub>red</sub>), eliminating the initial preheating and further decreasing system efficiency.

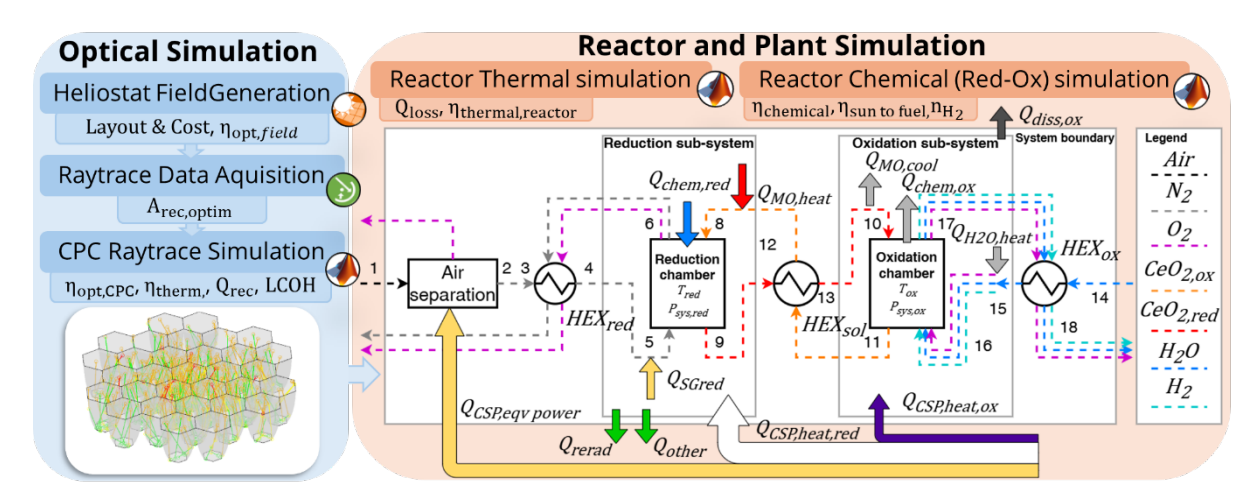
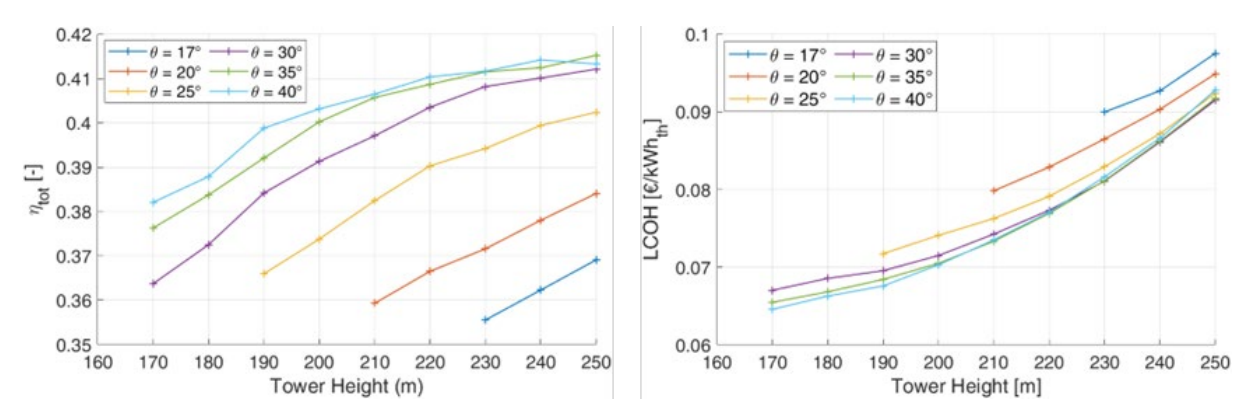


Figure 5. Methodology scheme of the optical and thermochemical optimization.

#### 3. Results

## 3.1 Single-receiver configuration

The results highlight the optimized tower configurations that achieve the highest optical and thermal efficiency (see *Figure 6*, left) for a range of semi-acceptance angles with optimum tower tilt and varying height. Values under  $\theta_{max}=17.5$  and 170 m of tower height were not able to reach design power. Additionally, the configurations that result in the lowest LCOH are shown (see *Figure 6*, right). These findings indicate that, at this power level, lower acceptance angles fail to meet the power target due to the limited heliostat field area. Furthermore, the results demonstrate that higher acceptance angles outperform lower ones for the selected power target, yielding better optical and thermal efficiencies. This efficiency gain, coupled with the ability to use lower tower heights, contributes to reduced LCOH values.



**Figure 6.** Left: overall yearly efficiency for a range of semi-acceptance angles with optimum tilt and varying height. Right: LCOH for a range of semi-acceptance angles with optimum tower tilt and height.

The case that yields the lowest LCOH (0.0646 €/kWh<sub>th</sub>) is found for a semi-acceptance angle of 40°, a tilt of 62.5° and a tower height of 170 m, which is the minimum tower height capable of delivering the design power to the receiver. The identified tower is selected to compute the thermochemical efficiency of the process. These results show a solar to hydrogen efficiency of 5.1%, in which the most significative losses are due to the enthalpy flows of the oxidation reactor that are not recovered and overall thermal losses in the system (see *Fig.* 7).

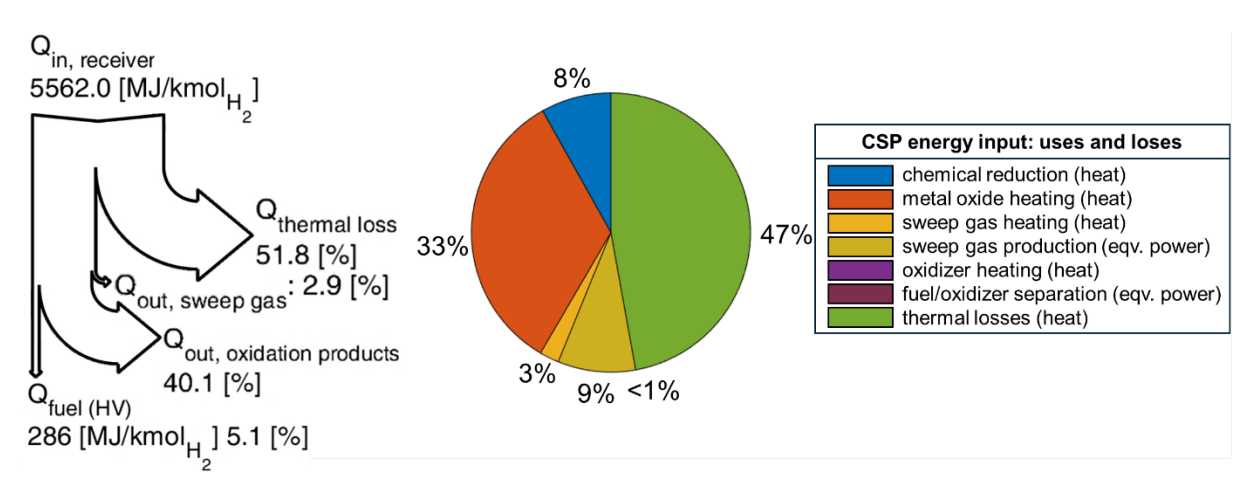
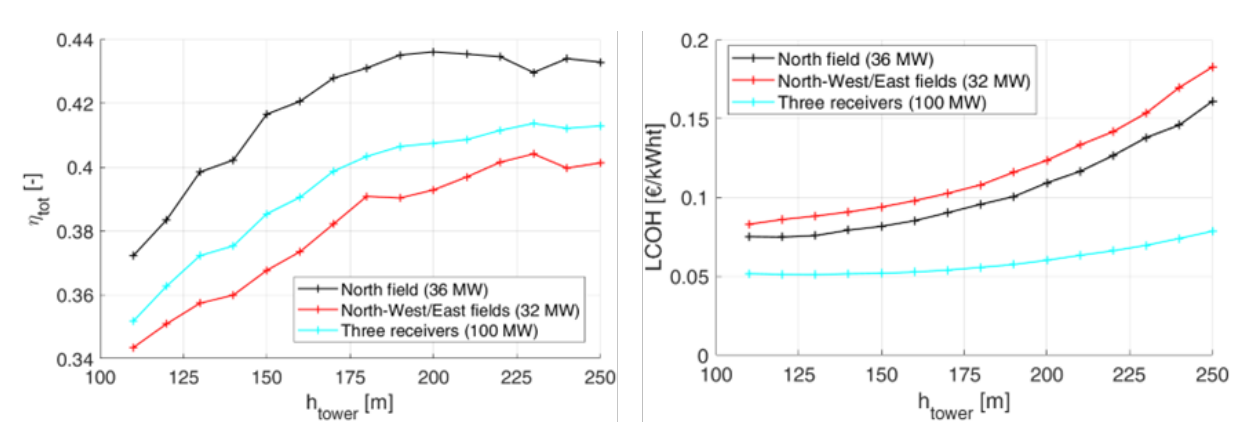


**Figure 7.** Left: Sankey diagram of the energy balance of the cycle per kmol of H2 produced. Right: Pie chart of the CSP heat usage of the system.

## 3.2 Three-receiver configuration

In the three-receiver configuration, the overall yearly optical and thermal efficiency for each receiver is calculated independently following the same principles as the previous case, selecting the optimum semi-acceptance angle in each sub-field. The total system efficiency is then determined by aggregating these individual efficiencies. Results reveal that the optimal LCOH and efficiency do not coincide. Specifically, LCOH tends to favor lower tower heights, whereas efficiency favors higher tower heights. A noticeable difference arises when comparing this configuration to the single north-facing receiver case. Since each receiver in the three-receiver setup is designed for a different power level, the optimal tower height for maximum efficiency varies accordingly. In the first scenario, the maximum tower height constraint prevented the identification of an optimal height, resulting in the maximum allowed height yielding the best performance. However, in the three-receiver configuration, an optimal efficiency is achieved at a lower tower height, beyond which efficiency begins to decline, as seen in *Figure 8*, left.

It can also be appreciated that, since the tower investment is shared among the three receivers, the LCOH is significantly reduced for the overall system, as seen in *Figure 8*, right. However, the individual fields exhibit slightly higher efficiencies, but also higher LCOH compared to the single-receiver case. This may be attributed to the reduced power levels and the limited area available for each field, as they share some of the same heliostat area.



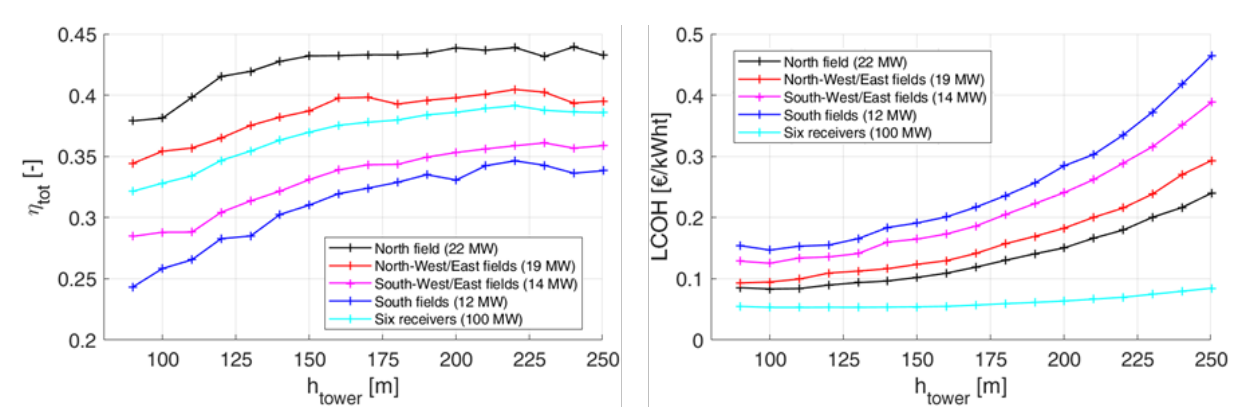
**Figure 8.** Results obtained for the best configurations ( $\theta_{max}$  and  $\beta$ ) by tower height on the three-receiver system. Left: Overall system yearly efficiencies. Right: LCOHs.

Table 2. Results obtained for the best configurations on the three-receiver system.

Parameter	N receiver	NW/NE receivers	3-receiver system	
h <sub>tower</sub> [m]	120	110	120	
θ <sub>max</sub> [°]	30	25	30/25	
β [°]	70	72.5	70/72.5	
η <sub>yearly</sub> [%]	38,35	34.36	35,80	
LCOH [€/kWh <sub>th</sub> ]	0.0749	0.0831	0.0507	
η <sub>sol-to-H2</sub> [%]	5.21	5.36	5.30	

#### 3.3 Six-receiver configuration

The conclusions drawn from the three-receiver configuration are also applicable to the six-receiver configuration, with a notable difference due to the lower power level of each individual receiver, as seen in *Figure 9*. However, despite the shared tower investment among six receivers, the efficiency of the south-facing receivers is so low that the overall LCOH of the full system does not improve compared to the three-receiver configuration. Another insight that can be drawn from these results is that the optimum semi-acceptance angle seems to decrease as the power level decreases.



**Figure 9.** Results obtained for the best configurations ( $\theta_{max}$  and  $\beta$ ) by tower height on the six-receiver system. Left: Overall system yearly efficiencies. Right: LCOHs.

**Table 3.** Results obtained for the best configurations on the six-receiver system.

Parameter	N	NW/NE	SW/SE	S	6-receiver
h <sub>tower</sub> [m]	100	90	100	100	100
$\theta_{max}[^{o}]$	25	25	20	20	25//20
β [°]	70	72.5	72.5	72.5	70//72.5
η <sub>yearly</sub> [%]	38.12	34.43	28.80	25.84	32.63
LCOH [€/kWh <sub>th</sub> ]	0.0833	0.0932	0.1253	0.1469	0.0532
η <sub>sol-to-H2</sub> [%]	5.25	5.26	5.07	5.00	5.17

#### 4. Conclusions

This study demonstrates the potential of an optimized 100 MW<sub>th</sub> CSP system, featuring a point-focus tower and CPCs, to enhance solar-to-hydrogen fuel conversion efficiency through a ther-mochemical cycle using non-stoichiometric ceria. By optimizing the optical configuration of the CSP system across different receiver setups, the research found that a single-receiver configuration resulted in the highest LCOH (0.0646 €/kWh<sub>th</sub>). However, a three-receiver setup proved more effective, lowering the LCOH to 0.0507 €/kWh<sub>th</sub> by distributing the tower investment across multiple receivers. In contrast, expanding to a six-receiver system was less efficient, as

the reduced power levels per receiver led to a higher LCOH (0.0531 €/kWh<sub>th</sub>). For comparison, literature reports LCOH values as low as 0.046 USD/kWh<sub>th</sub> for single cavity receivers operating at 850–1100 °C [12], and down to 0.021 USD/kWh<sub>th</sub> under even lower operating temperatures such as 500 °C with central receivers [13]. These discrepancies are primarily attributed to differences in operating temperature, among other design factors. Although the thermochemical efficiency was computed for each configuration, no significant differences were observed, with the three-receiver configuration achieving the highest efficiency at 5.3%. Ultimately, the findings underscore the importance of strategic receiver placement and concentration management in optimizing solar fuel production systems.

## Data availability statement

Data will be available under request.

#### **Author contributions**

**Alejandro González Silvestre:** Formal analysis, Investigation, Software, Visualization, Writing – original draft. **Gioele di Marcoberardino:** Supervision, Writing – review & editing, Project administration. **Marco Binotti:** Supervision, Writing – review & editing, Project administration.

## **Competing interests**

The authors declare that they have no competing interests.

# **Funding**

This work was funded by the Marie Skłodowska-Curie Actions doctoral network within the TOP-CSP project (GA No. 101072537).

#### References

- [1] C. Moretti, V. Patil, C. Falter, L. Geissbühler, A. Patt and A. Steinfeld, "Technical, economic and environmental analysis of solar thermochemical production of drop-in fuels" Science of the Total Environment, vol. 901, 25 November 2023, doi: <a href="https://doi.org/10.1016/j.scitotenv.2023.166005">https://doi.org/10.1016/j.scitotenv.2023.166005</a>
- [2] V.K. Budama, J.P.R. Duarte, M. Roeb, C. Sattler, "Potential of solar thermochemical water-splitting cycles: A review" Solar Energy, Volume 249, Pages 353 366, 1 January 2023, doi: <a href="https://doi.org/10.1016/j.solener.2022.11.001">https://doi.org/10.1016/j.solener.2022.11.001</a>.
- [3] Y. Lu, L. Zhu, C. Agrafiotis, J. Vieten, M. Roeb, and C. Sattler, "Solar fuels production: Two-step thermochemical cycles with cerium-based oxides," *Progress in Energy and Combustion Science*, vol. 75. Elsevier Ltd, Nov. 01, 2019. doi: <a href="https://doi.org/10.1016/j.pecs.2019.100785">https://doi.org/10.1016/j.pecs.2019.100785</a>.
- [4] Bhosale RR, Takalkar G, Sutar P, Kumar A, AlMomani F, Khraisheh M, "A decade of ceria based solar thermochemical H2O/CO2 splitting cycle", *International Journal of Hydrogen Energy*, Volume 44, Issue 1, 2019, Pages 34-60, ISSN 0360-3199, doi: https://doi.org/10.1016/i.iihydene.2018.04.080.
- [5] J.-P. Säck, S. Breuer, P. Cotelli, A. Houaijia, M. Lange, M. Wullenkord, C. Spenke, M. Roeb, C. Sattler "High temperature hydrogen production: Design of a 750 KW demonstration plant for a two step thermochemical cycle", Solar Energy, Volume 135, October 2016, Pages 232-241, doi: <a href="https://doi.org/10.1016/j.solener.2016.05.059">https://doi.org/10.1016/j.solener.2016.05.059</a>
- [6] M. Schmitz, P. Schwarzbözl, R. Buck, R. Pitz-Paal, "Assessment of the potential improvement due to multiple apertures in central receiver systems with secondary concentrators", Solar Energy 80 (2006) 111–120, doi: <a href="https://doi.org/10.1016/j.solener.2005.02.012">https://doi.org/10.1016/j.solener.2005.02.012</a>

- [7] National Renewable Energy Laboratory. SolarPILOT & SolTrace.
- [8] The MathWorks, Inc., Natick, Massachusetts, U. S. MATLAB®, R2019b.
- [9] A. Giostri. "Preliminary analysis of solarized micro gas turbine application to CSP parabolic dish plants", Energy Procedia, Volume 142, December 2017, Pages 768-773, doi: <a href="https://doi.org/10.1016/j.egypro.2017.12.124">https://doi.org/10.1016/j.egypro.2017.12.124</a>
- [10] S. Li, V.M. Wheeler, P.B. Kreider, R. Bader, and W. Lipiński. "Thermodynamic Analyses of Fuel Production via Solar-Driven Non-stoichiometric Metal Oxide Redox Cycling. Part 2. Impact of Solid-Gas Flow Configurations and Active Material Composition on System-Level Efficiency." Energy & Fuels, vol. 32, no. 10, pp.10848-10863, 1 October 2018, doi: <a href="https://doi.org/10.1021/acs.energyfuels.8b02082">https://doi.org/10.1021/acs.energyfuels.8b02082</a>
- [11] M. Binotti, G. di Marcoberardino, M. Biassoni, G. Manzolini. "Solar hydrogen production with cerium oxides thermochemical cycle" SolarPACES 2016 AIP Conf. Proc. 1850, 100002-1–100002-10; doi: https://doi.org/10.1063/1.4984459
- [12] P. Ingenhoven, L. Lee, W. Saw, M.M. Rafique, D. Potter, G.J. Nathan "Techno-economic assessment from a transient simulation of a concentrated solar thermal plant to deliver high-temperature industrial process heat", Renewable and Sustainable Energy Reviews 185 (2023) 113626, doi: https://doi.org/10.1016/j.rser.2023.113626
- [13] G. Gentile, G. Picotti, M. Binotti, M.E. Cholette, G. Manzolini, "A comprehensive methodology for the design of solar tower external receivers" Volume 193, April 2024, 114153. doi: https://doi.org/10.1016/j.rser.2023.114153